IEEE Journal of Solid-State Circuits, Vol. 47, No. 10, pp. 2372-2384, Oct. 2012.

A 2.4-GHz, 27-dBm Asymmetric Multilevel Outphasing Power Amplifier in 65-nm CMOS

Philip A. Godoy, *Member, IEEE,* SungWon Chung, *Student Member, IEEE,* Taylor W. Barton, *Student Member, IEEE,* David J. Perreault, *Senior Member, IEEE* and Joel L. Dawson, *Member, IEEE*

Abstract

We present a 2.4-GHz asymmetric multilevel outphasing (AMO) power amplifier (PA) with class-E branch amplifiers and discrete supply modulators integrated in a 65-nm CMOS process. AMO PAs achieve improved modulation bandwidth and efficiency over envelope tracking (ET) PAs by replacing the continuous supply modulator with a discrete supply modulator implemented with a fast digital switching network. Outphasing modulation is used to provide the required fine output envelope control. The AMO PA delivers 27.7-dBm peak output power with 45% system efficiency at 2.4-GHz. For a 20-MHz WLAN OFDM signal with 7.5-dB PAPR, the AMO PA achieves a drain efficiency of 31.9% and a system efficiency of 27.6% with an EVM of 2.7%-rms.

Index Terms

power amplifier, outphasing, LINC, discrete supply modulator, digital predistortion

Manuscript received November 8, 2011; revised March 10, 2012. This work was funded in part by the MIT Deshpande Center and by the MIT Center for Integrated Circuits and Systems.

P. A. Godoy, S. Chung, T. W. Barton, D. J. Perreault, and J. L. Dawson are with the Department of Electrical Engineering and Computer Science, Massachusetts Institute of Technology, Cambridge, MA 02139 USA (e-mail: godoy@mit.edu; sungwon@mit.edu; tbarton@mit.edu; djperrea@mit.edu; jldawson@mtl.mit.edu).

IEEE Journal of Solid-State Circuits, Vol. 47, No. 10, pp. 2372-2384, Oct. 2012.

I. Introduction

The demand for increased communication data rates with wideband, high peak-to-average power ratio (PAPR) modulated signals is complicated by a competing need for high-efficiency performance. Tremendous efforts to beat the linearity-efficiency tradeoff for PAs have led to a wide variety of architectures. One potential solution is the outphasing system, also known as linear amplification with nonlinear components (LINC) [1], [2]. In the outphasing system, shown in Fig. 1(a) an input signal containing both amplitude and phase modulation is divided into two constant-envelope phase-modulated signals [3]. An amplified version of the original signal is achieved by varying the phases of these two signals and summing the amplified branch signals with a passive power combiner. The maximum envelope is obtained when the branches are in-phase, while the minimum envelope is obtained when the branches are antiphase. The advantage of this technique is that highly efficient nonlinear PAs can be used to amplify the two constant envelope signals, increasing the overall efficiency without degrading linearity.

Outphasing architectures are capable of transmitting very wideband signals and are thus suitable for wideband communication in multi-standard applications. However, one of the major disadvantages of the LINC architecture is the power wasted in the power combiner. To avoid signal distortion and preserve switching amplifier efficiency, an isolating combiner such as a Wilkinson combiner should be used, which isolates the two outphased PAs and provides a fixed load impedance to each PA. Isolating combiners achieve 100% efficiency only at maximum output power. When the inputs are outphased to vary the amplitude, power is wasted as heat in the isolation resistor [3], as shown in Fig. 1(a).

To alleviate the problem of wasted energy during outphasing, nonisolating combiners are sometimes used. One example is the Chireix combiner, which uses compensating reactive elements to enhance the power-combining efficiency [1], [3]–[5]. However, the Chireix combiner can only be tuned for a very small range of outphasing angles. Outside the tuned range, the load impedance presented to the PAs deviates too far from the nominal value, resulting in significant distortion and degraded PA efficiency. Adaptive termination of each amplifier output depending on the outphasing angle was applied in [6] to improve the combiner efficiency over a much larger range of outphasing angles. However, the frequency dependence of the time-varying load presented to the PAs can complicate efforts to transmit wideband signals. Good linearity can also be achieved with a non-isolating combiner if class-D or class-F PAs are used, which behave more like voltage sources and so are less sensitive to load impedance variation [7], [8]. However, class-F PAs cannot achieve 100% theoretical efficiency (like other switching PAs) unless all harmonics are terminated [9], which would cost a lot of area. Class-D PAs typically have lower efficiency than other switching PAs due to the additional PMOS device, increasing gate and drain capacitance and resulting in higher loss [10].

Another potential solution to the efficiency/linearity tradeoff is polar and envelope tracking (ET) amplifiers. The fundamental idea of polar architectures, shown in Fig. 1(b), is to divide the signal to be amplified into amplitude and phase components. The phase component is used as the input to a nonlinear, high-efficiency switching PA, while the amplitude component drives the power supply of the PA to create a varying-envelope signal [11]–[13]. While this improves the PA efficiency, it also requires the use of an efficient power converter for the amplitude modulator. Because power converter efficiency degrades significantly as bandwidth increases, it is very difficult to achieve high efficiency and high bandwidth simulataneously. This is exacerbated by the 5-10x bandwidth expansion that occurs during the conversion from Cartesian to polar coordinates [14]. Thus, this method is typically only effective for low-bandwidth systems. Various supply modulators such as the class-G modulator [15], two-point supply modulator [16], [17], and $\Delta\Sigma$ supply modulator [18], have been developed. However, all of these modulators still have the problem of suffering from a tradeoff between high linearity and wideband supply modulation.

To overcome the shortcomings of the outphasing and polar architectures, asymmetric multilevel outphasing (AMO) has been proposed as a hybrid of the outphasing and polar architectures for high-efficiency wideband RF transmission [19]–[23]. Shown in Fig. 2, AMO combines outphasing with discrete supply modulation. The problem of wasted power in the combiner is alleviated by lowering the supply voltage of the two outphased PAs for small output envelopes, reducing the DC power dissipation. At the same time, the problem of limited supply-modulation bandwidth is alleviated by replacing the continuous supply modulator with a discrete one, implemented with a fast, digital switching network that achieves both high speed and high efficiency simultaneously. The AMO system only requires discrete amplitude modulation because it is only used for coarse amplitude control; fine amplitude control is achieved using outphasing. This work presents the highest-performance CMOS implementation of the AMO concept to date. Compared to the previous AMO CMOS PA presented [22], this work achieves significantly higher output power, modulation bandwidth, and efficiency.

The outline of this paper is as follows. In Section II, we describe AMO concept, including the required signal decomposition for AMO modulation and the theoretical efficiency of the system. Section III describes the static predistortion algorithm used to correct for the nonlinearities in the AMO system. The details of the AMO PA implementation are given in Section IV, and Section V presents the measurement results. Finally, we present our conclusions in Section VI.

II. AMO System

A. AMO Modulation

Fundamentally, AMO modulation decomposes a complex vector, which represents a baseband constellation point, into two vectors such that the sum of the two vectors constructs the original complex vector with the *minimum* outphasing angle, as illustrated in Fig. 3. The two vectors are the baseband representation of the two PA outputs. Mathematically, AMO modulation decomposes an arbitrary RF output signal $S_{out}(t)$ into two constant-envelope signals $S_1(t)$ and

$S_2(t)$ such that the sum constructs the original signal. $S_{out}(t)$ can be defined in terms of either Cartesian or polar coordinates as

$$S_{out}(t) = I(t)\cos(\omega t) + Q(t)\sin(\omega t) = A(t)\cos(\omega t + \phi(t)) \tag{1}$$

where $I(t)$ and $Q(t)$ are the in-phase and quadrature components, respectively, of the RF signal being transmitted, $A(t)$ and $\phi(t)$ are the amplitude and phase components, respectively, and ω is the RF carrier frequency. For fixed PA amplitudes A_1 and A_2 for the two PAs in the AMO system, the AMO signal decomposition can be performed by referring to the vector diagram shown in Fig. 3 and using the law of cosines, resulting in the following equations:

$$S_{out}(t) = S_1(t) + S_2(t) = A_1(t)\cos[\omega t + \phi_1(t)] + A_2(t)\cos[\omega t + \phi_2(t)] \tag{2}$$

$$\phi_1(t) = \phi(t) + \cos^{-1}\left[\frac{A_1(t)^2 + 2A(t)^2 - A_2(t)^2}{4A_1(t)A(t)/\sqrt{2}}\right] \tag{3}$$

$$\phi_2(t) = \phi(t) - \cos^{-1}\left[\frac{A_2(t)^2 + 2A(t)^2 - A_1(t)^2}{4A_2(t)A(t)/\sqrt{2}}\right] \tag{4}$$

$$\theta(t) = \phi_1(t) - \phi_2(t) \tag{5}$$

$\phi_1(t)$ and $\phi_2(t)$ are the phases of the two PAs, and $\theta(t)$ is called the *outphasing angle*. For a given vector $S_{out}(t)$, there are multiple choices for the PA amplitudes and phases $A_1(t)$, $A_2(t)$, $\phi_1(t)$, and $\phi_2(t)$. For any given desired amplitude A and phase ϕ, we choose A_1, A_2, ϕ_1, and ϕ_2 to minimize the energy lost in the isolation port of the power combiner.

B. Theoretical Efficiency

To calculate the efficiency of the AMO system, we must first calculate the efficiency of the isolating power combiner for the case when the two input signals being combined are not the same power level (i.e., asymmetric power combining). In this case, there is loss in the combiner even when there is no outphasing (i.e., $\phi_1 = \phi_2$). This is because an isolating combiner has two output ports, one for the sum of the two input signals and one for the difference. When the input amplitudes are different, some of the power goes to the difference port even if the phases are the same. The difference port is normally terminated with a resistor, so that this power is wasted as heat and the efficiency is no longer 100%. The efficiency of power combining with an ideal isolating power combiner is

$$\eta_c = \frac{(A_1 \cos\theta_1 + A_2 \cos\theta_2)^2}{2\left({A_1}^2 + {A_2}^2\right)} \tag{6}$$

where A_1 and A_2 are the amplitudes of the two RF sinusoid inputs whose phases are θ_1 and θ_2 relative to the output phase (see Fig. 3).

In the AMO system, if there are N different PA output amplitudes A_1 to A_N, there are $\binom{N}{2} + N$ combinations of PA amplitudes for the two PAs (assuming no mismatch between the two PAs). However, as can be seen in Eq. 6, the combiner efficiency decreases as the difference between two amplitude levels increases. Therefore, in our implementations of the AMO system, we restrict the combinations to be adjacent amplitude levels (i.e., A_k and A_{k+1}).

Fig. 4 shows the theoretical efficiency vs. output power for the AMO system when there are 4 amplitude levels available vs. when there are 2 amplitude levels available. Note that the AMO system gives a significant efficiency improvement over the standard outphasing system, and that the greater the number of amplitude levels, the higher the efficiency curve over a given output power range. However, as the number of amplitude levels increases, so does the complexity of the discrete amplitude modulators. Note that there is an efficiency peak corresponding to each possible combination of the amplitude levels for the two outphased PAs, with the restriction that we choose the PA supply levels to be either identical or to differ at most by one level.

It should be noted that there is an efficiency and area penalty associated with generating the multiple supply voltages required by the AMO system. However, a multi-level DC-DC converter can still achieve a reasonably high efficiency with a compact size. For example, a multi-level DC-DC converter with 4 outputs has been reported in [24] that achieves over 90% efficiency occupying a CMOS die size of 1.8 mm x 2.1 mm and only 1 off-chip inductor, thus adding no additional off-chip components compared to a conventional single-channel DC-DC converter.

C. Multi-standard Efficiency Optimization

For a given signal's amplitude probability density function (PDF), we can choose the values of the amplitude levels in the AMO system such that the overall average efficiency is maximized. In this way, we can optimize the AMO system for multiple wireless communication standards simply by changing the PA supply voltages. The optimum values of the supply voltages can be determined as follows. Let us define the output amplitude levels r_k to be the maximum output amplitudes for each of the different supply voltage levels $V_{sup,k}$ when both PAs are driven by the same supply[1]. Let us also define $n_{PA}(r_k)$ to be the PA efficiency when the output amplitude is r_k (with both PAs driven by the same supply)[2]. Fig. 5 shows an example amplitude PDF for a modulated signal, along with an example PA efficiency curve vs. output amplitude. The total average efficiency can be computed as

$$\eta_{avg} = \frac{\langle Pout \rangle}{\langle P_{DC} \rangle} \tag{7}$$

If the amplitude PDF $p(A)$ of the signal is known, then the average output power is simply

$$\langle P_{out} \rangle = \int p(A) A^2 dA \tag{8}$$

To determine the average DC power, we divide the PDF into several regions separated by the r_k (and their combinations), and for each region we integrate the PDF curve to find the total probability in that region and multiply that probability by the DC power consumption when the

[1]In this analysis, we assume there is no mismatch between the two PAs for simplicity. In practice, this assumption does not impact performance very much as long as the mismatch is not severe

[2]$n_{PA}(r_k)$ should include the loss of the DC-DC converter providing the supply voltage to the PA.

AMO system operates in that region (see Fig. 5). With the combinations of supply voltages restricted to be adjacent supply levels, the average DC power can be computed as

$$\langle P_{DC}\rangle = \frac{r_1^2}{\eta_{PA}(r_1)}\int_0^{r_1} p(A)dA$$
$$+\sum_{k=1}^{N-1}\left[\frac{1}{2}\left(\frac{r_k^2}{\eta_{PA}(r_k)}+\frac{r_{k+1}^2}{\eta_{PA}(r_{k+1})}\right)\int_{r_k}^{\frac{r_k+r_{k+1}}{2}} p(A)dA\right.$$
$$\left.+\frac{r_{k+1}^2}{\eta_{PA}(r_{k+1})}\int_{\frac{r_k+r_{k+1}}{2}}^{r_{k+1}} p(A)dA\right] \tag{9}$$

Using this equation, the optimum set of supply voltage levels for a given amplitude PDF can be found by first measuring the PA efficiency $n_{PA}(r_k)$ as a function of r_k (sweeping the supply voltage), and then performing an exhaustive search on the N values of the r_k.

Fig. 6(a) shows the amplitude PDF for an HSUPA signal (a 3G cellular standard) and the corresponding optimum efficiency curves for LINC and AMO using 4 different supply levels. The data was generated using Agilent's ADS software, and the PA efficiency curve was obtained from simulation of a class-E PA designed in a 65-nm CMOS process. The figure shows that AMO increases the efficiency over a much wider power range than the standard LINC system. Fig. 6(b) shows the amplitude PDF and optimum efficiency curves for a WLAN signal.

III. AMO Static Predistortion Algorithm

Section II-A described the mathematical signal decomposition for AMO modulation that determines the amplitudes and phases for the two outphasing branches. However, this decomposition will not be accurate if there is amplitude and phase mismatch between the two branches. Some mismatch will always occur in real systems due to random variation and component tolerances. Applying the formulation in Section II-A with two mismatched paths would result in a distorted output signal. Furthermore, the AMO signal decomposition requires the values of the PA amplitude levels A_k to be known ahead of time. It is hard to accurately predict what the PA amplitude levels will be based on the supply voltage alone. This is due to the nonlinearity of the PA output amplitude as a function of the supply voltage, which is well-known in polar-modulation architectures [13], [25]. The PA output phase also varies with supply voltage, which is not accounted for in the ideal AMO signal decomposition of Section II-A. For these reasons, some method of linearization or digital predistortion (DPD) based on measurements of the PA output is required to correct for the nonlinearities in a real AMO system.

For this work, we implement an AMO DPD method based on lookup table training [26], [27]. The first step is to measure the PA output amplitude and phase vs. outphasing angle for each possible combination of amplitude levels for the two outphased PAs. For example, if there are 4 amplitude levels available, there would be 7 possible combinations as described in Section II-B. Specifically, referring to Fig. 2, we set the inputs to the AMO system as follows:

$$A_1 = V_i, \qquad A_2 = V_j, \qquad \phi_1 = \frac{\theta}{2}, \qquad \phi_2 = -\frac{\theta}{2} \tag{10}$$

V_i and V_j represent the available amplitude levels for the PAs, and θ is defined as the outphasing angle, which can range from -180° to +180°. With these input settings, we measure the amplitude and phase of the output S_{out}, sweeping θ. We do this for every combination of amplitude levels for the two PAs (V_i and V_j). Note that negative and positive outphasing angles can yield different measurement results due to the amplitude and phase mismatch between the two outphasing paths.

The measurements of the output amplitude and phase vs. outphasing angle capture the amplitude and phase distortions of the system due to the mismatch between the 2 outphasing paths as well as the varying supply voltage. An example of this measurement data is given in Fig. 7, which shows the measurement results for the 2.4-GHz AMO PA presented in this work. There are 7 different curves, each for a different combination of amplitude levels for the two outphased PAs. Note that not all outphasing angles are measured for every possible combination. This is because we only require that all the curves together cover the entire amplitude range. As described in Section II-A, there are multiple solutions for the PA amplitude and phases that yield the same output amplitude. The combinations with the lowest amplitude levels are favored over the others, because they result in the lowest DC power dissipation and therefore the highest efficiency. Fig. 8 gives the amplitude and phase linearity plots for the measurement data given in Fig. 7. Fig. 8(a) plots the difference between the measured output phase and the ideal input phase, plotted vs. the ideal input amplitude. Fig. 8(b) plots the measured output amplitude vs. the ideal input amplitude. The ideal input amplitudes and phases are the result from the ideal AMO signal decomposition given in Section II-A.

Once the distortion data has been measured, the AMO signal decomposition with DPD proceeds as shown in Fig. 9. The algorithm is as follows:

1) **Cartesian to Polar Conversion:** The baseband I and Q data is converted to polar coordinates A and ϕ.
2) **Amplitude Level Selection:** The combination of amplitude levels for the two outphased PAs (A_1 and A_2) is chosen based on A, using the measured amplitude data collected before. As mentioned previously, the combination with the lowest amplitude levels is chosen for maximum efficiency. For example, using the data in Fig. 7, if the normalized A was 0.8, the combination (V4,V3) would be chosen for (A_1,A_2).
3) **Amplitude LUT:** The outphasing angles that resulted in the given A for the previously chosen amplitude combination are recorded. Note that there are always two possible outphasing angles, θ_A and θ_B, for a given A; typically one is positive and the other is negative, as shown in Fig. 7.
4) **Phase LUT:** The corresponding output phase offsets, $\phi_{os,A}$ and $\phi_{os,B}$, for the two possible outphasing angles, θ_A and θ_B, are recorded.
5) **Phase Calculation:** The phases for the two PAs, ϕ_1 and ϕ_2, are calculated as follows:

$$\phi_1 = \phi + \frac{\theta}{2} + \phi_{os}, \qquad \phi_2 = \phi - \frac{\theta}{2} + \phi_{os} \tag{11}$$

Note that there will be two possible solutions for the PA phases, ($\phi_{1,A}$,$\phi_{2,A}$) and ($\phi_{1,B}$,$\phi_{2,B}$), corresponding to the two possible solutions for θ and ϕ_{os}.

6) **Optimal Outphasing Assignment:** The final step is to choose one of the two possibilities for the PA phases. To make this decision, we use the optimal outphasing assignment scheme described in [28], [29]. Basically, this involves calculating the phase difference between the current sample and the previous sample for both ϕ_1 and ϕ_2. The previous sample has already been chosen, but the current sample has two possibilities. The possibility that minimizes the worst-case phase difference for ϕ_1 and ϕ_2 is chosen. Large, abrupt phase changes are undesirable because the finite bandwidth of phase modulators and the PA input and output matching networks filter out these abrupt changes so that the linearity and noise of the system is degraded. Fig. 10 shows the PA phases and phase differences after the AMO signal decomposition with and without the optimal outphasing assignment. The input data is a 16-QAM signal, and the constellation diagram and trajectory of the 16-QAM signal is also shown. It can be seen that the optimal outphasing assignment significantly reduces the magnitude of the abrupt phase changes.

Fig. 11 shows the time-domain waveforms of the PA amplitudes and phases, A_1, A_2, ϕ_1, ϕ_1, for a segment of the 16-QAM signal shown in Fig. 10(a). They are the result from the AMO signal decomposition with DPD outlined above, using the measured data shown in Fig. 7. It can be seen that the two PA amplitude levels closely follow the amplitude of the input signal, so that the DC power consumption is minimized for the highest possible efficiency. Also note the outphasing angle remains relatively small, except when the amplitude becomes very small.

IV. AMO PA IMPLEMENTATION

The AMO PA was implemented in a 65-nm RF CMOS process and designed to operate at 2.5 GHz. Both the discrete supply modulator and PA were integrated on the chip, and the circuit schematic for these blocks are shown in Fig. 12. The PA can switch among 4 different supply voltages, which come from external power supplies. The power supply switches are thick-oxide devices to pass supply voltages up to 2.5 V. They consist of both NMOS and PMOS devices in parallel and are designed for low on-resistance to minimize DC power dissipation. The large gate capacitances of the power supply switches are driven with a chain of 2.5-V inverters. All the digital logic for the digital amplitude data is implemented with thin-oxide, 1.0-V devices for lower power dissipation. Level shifters convert the digital control signals from the 1.0-V to the 2.5-V domain. All the switch select signals are clocked for synchronization, and the clock signal has a variable delay to perform time alignment between the AM and PM paths.

Although Fig. 12 shows a single-ended PA, the PA is differential on chip. The PA operates as sub-optimum class-E [30], [31], which has a lower peak drain voltage compared to standard class-E. This allows for a higher maximum supply voltage, resulting in a higher overall efficiency. The PA uses a thick-oxide cascode transistor (M2) to further increase the maximum supply voltage, while the main switch (M1) is a thin oxide device for faster switching and lower driver loss. The choke inductor is an integrated spiral inductor, while the output matching network uses the bondwire inductance from the chip packaging along with off-chip capacitors. The cascode gate is biased using a modified version of the self-biasing scheme used in [32], [33], in which the cascode bias tracks the supply voltage for higher efficiency at power backoff. The gate of the main switch is driven with an inverter chain to provide a square-wave input to the class-E PA.

In the AMO system, when the PA supply voltage switches levels, the PA supply node experiences transient ringing due to the parasitic capacitances of the switches together with the bondwire inductance from the chip packaging. Shown in Fig. 13, this ringing is undesirable because it causes glitches in the output waveform whenever the supply voltages are switched, increasing the noise in the output signal. Ringing also occurs on the supply voltage of the buffers driving the large switch gate capacitance. Flip-chip packaging can help mitigate this problem by reducing the inductance, but only to a certain extent and at additional cost. Adding on-chip bypass capacitance to each power supply voltage can also help; however, due to the high currents drawn by the PA, the required capacitance is usually too large for integration. Instead, we reduce the ringing by adding a damping leg to each power supply input, consisting of a series resistor and capacitor. The simulation results shown in Fig. 13 demonstrate that this significantly reduces the power supply ringing compared to using just bypass capacitance or no damping leg at all.

Due to limited chip area, only 1 branch of the outphasing system is fabricated on a single chip; 2 different chips are combined to form the total AMO system. Fig. 14 shows the die photo. The entire chip is 2×2 mm^2, but the active area used for the PA, discrete supply modulator, buffers, and digital logic is about 1×1 mm^2. The testbench is shown in Fig. 15. The 2 phase modulators are each implemented with a 16-bit dual-channel DAC evaluation board from Analog Devices (AD9779A), which includes an I/Q modulator (ADL5375) to upconvert the baseband data to the RF carrier frequency. The 2 differential PA outputs are converted to single-ended signals with off-chip baluns, and then fed into an isolating Wilkinson combiner. To correct for the static nonlinearities of the AMO system due to branch mismatch and the varying PA supply voltage, the static digital predistortion method described in Section III is applied. The digitally predistorted baseband data is generated in MATLAB and then uploaded to an FPGA to provide the digital inputs to the amplitude and phase modulators at a sampling rate of 200 MHz.

V. Measurement Results

Fig. 16 shows the measured efficiency vs. output power for the AMO PA, which includes the power from the predriver and all preceding buffers. The peak output power was measured to be 27.7 dBm at 2.4 GHz with a peak efficiency of 45%. Note that all output power and efficiency numbers include the loss from the off-chip baluns and power combiner, which together give about 1 dB insertion loss. This loss is comparable to the loss of an on-chip power combiner [34], [35] (an off-chip balun for each PA would not be required in this case because the on-chip combiner can perform the differential to single-ended conversion). Although there would be an area penalty for an on-chip combiner, it would enable higher total output power, which is a major difficulty for CMOS PAs.

The curve labeled “VDD” in Fig. 16 shows the efficiency as the supply voltage is varied continuously for both PAs together. We cannot operate directly on this curve because it would require continuous supply modulation. Instead we use the AMO system, which combines discrete supply modulation with outphasing. The curve labeled “AMO” gives the resulting efficiency with 4 supply-voltage levels. Note that the AMO system maintains a high efficiency over a wide output-power range. The supply-voltage levels chosen in the plot are optimized for a 64-QAM signal with a PAPR of 7.0 dB, the PDF of which is shown in the same plot. The 4 supply voltages used in this work are 2.5, 1.8, 1.35, and 0.85 V.

The top two plots of Fig. 17 show the measured step response of the AMO PA output for an AM (supply voltage) step and a PM (outphasing angle) step. The AM step response settles in 3 ns, demonstrating the relatively fast speed of the discrete supply modulator. The PM step response settles in 6 ns and is limited by the finite bandwidth of the phase modulator. Since the AMO system requires abrupt AM/PM changes when the supply voltage is switched, the nonzero settling time causes glitches in the output waveform that degrade linearity and add noise to the output signal. This can be seen in the bottom two plots of Fig. 17, which show the AMO PA output for a 1-MHz baseband sine wave. Note that there are glitches in the output waveform when the AMO system is used that are not present when the LINC system is used, which occur when the supply voltages change levels. Because the phase path currently limits the speed of the system, a phase modulator optimized for speed such as the one presented in [36] could be used to achieve better performance.

To validate the performance of the AMO system for wireless data transmission, a 64-QAM signal was transmitted with the AMO PA at various symbol rates. Fig. 18 shows the constellation diagrams for 10-MHz and 40-MHz symbol rates. As explained above, the EVM degrades at higher symbol rates due to the finite settling time of the output when the PA amplitudes and phases change abruptly in the AMO system. However, even the worst-case EVM of 2.5% is acceptable for most applications.

Fig. 19(a) shows the average system efficiency and EVM of the AMO PA for the 64-QAM signal transmission with various channel bandwidths from 5 to 40 MHz. For comparison purposes, we also show the results for the LINC case, when only a single supply voltage is used for both PAs. From the plot, we can see a significant improvement in the efficiency for 4-level AMO vs. LINC, from 9% to almost 30%, an efficiency improvement of 3x. The efficiency of the AMO system drops slightly at higher symbol-rates due to the dynamic losses from the discrete supply modulator, but the efficiency degradation is very small, demonstrating the high efficiency of the discrete supply modulators. This can be more clearly seen in Fig. 19(b), which gives the power breakdown of the 64-QAM signal transmission at the various symbol rates. Note that the power loss is small compared to the other sources of power loss in the system, and that the power loss does not increase significantly as the symbol-rate increases. The high efficiency of the discrete supply modulators demonstrates the potential of the AMO system to achieve both high-efficiency and high-bandwidth wireless transmission.

Fig. 20 show the spectrum of the 64-QAM signal transmission at 10-MHz and 40-MHz symbol rates for both the LINC and AMO cases. The curves labeled "DAC" show the spectrum using just the phase modulators without the PAs; these are shown as a reference for the input signal driving the AMO system. It can be seen that at 10-MHz symbol rate, the noise floor of the AMO system is about 10dB higher than the LINC system. Again, this is due to the finite settling time of the PAs in response to the abrupt amplitude/phase changes, causing glitches in the output waveform which show up as a higher noise floor. At 40-MHz symbol rate, the AMO case is only slightly worse than the LINC case, suggesting that at these high bandwidths the system is limited by the finite bandwidth of either the phase modulator or the PA itself. The noise floor can be improved by optimizing the phase modulation path for a faster settling time.

We also tested the AMO PA with a 20-MHz WLAN signal (64-QAM OFDM) with a PAPR of 7.5 dB. Fig. 21 shows the measured constellation and output spectrum for this signal. At 20.2-dBm output power, the AMO PA achieves an EVM of 2.7%-rms with 27.6% drain efficiency and 27.6% system efficiency. To the authors' best knowledge, this is the highest reported efficiency in the literature for a CMOS PA in the 2-2.7 GHz frequency range for signal bandwidths greater than 10 MHz. Table I compares the efficiency of the AMO PA with other published works.

Fig. 22 shows the wideband output spectrum of the 20-MHz WLAN signal transmission shown in Fig. 21. As in the previous spectrum plots, the higher noise floor for the AMO case is evident. The spectral replicas appearing at 200-MHz steps away from the carrier frequency are due to the 200-MHz sampling rate of the digital input data driving the phase modulators. These spectral replicas violate the WLAN spectral mask; however, they can be suppressed by using a higher-order baseband low-pass filter (LPF) at the output of the transmit DACs (the ADI DAC evaulation boards used in our testbench have only a 3rd-order filter). The sampling rate of the phase modulators can also be increased to push the spectral replicas further away from the carrier frequency where they would be more strongly attenuated (in this work, the sampling rate was limited to 200-MHz by the FPGA testbench.)

VI. Conclusion

We present a 2.4-GHz AMO PA with class-E branch amplifiers and discrete supply modulators integrated in a 65-nm CMOS process. The AMO PA uses discrete supply-voltage modulation for fast and efficient coarse-amplitude control, and outphasing for fine-amplitude control. The 4-level AMO system delivers 27.7-dBm peak output power with 45% system efficiency. For a 20-MHz WLAN OFDM signal with 7.5-dB PAPR, the AMO PA achieves 31.9% drain efficiency and 27.6% system efficiency with an EVM of 2.7%-rms.

ACKNOWLEDGMENT

The authors wish to thank the TSMC University Shuttle Program for the fabrication of this design.

REFERENCES

[1] H. Chireix, "High-power outphasing modulation," *Proc. IRE*, vol. 23, pp. 1370–1392, Nov. 1935.

[2] D. C. Cox, "Linear amplification with nonlinear components," *IEEE Trans. Commun.*, vol. COM-23, pp. 1942–1945, Dec. 1974.

[3] I. Hakala, D. K. Choi, L. Gharavi, N. Kajakine, J. Koskela, and R. Kaunisto, "A 2.14-GHz Chireix outphasing transmitter," *IEEE Trans. Microwave Theory and Tech.*, vol. 53, no. 6, pp. 2129–2138, June 2005.

[4] F. H. Raab, "Efficiency of outphasing RF power-amplifier systems," *IEEE Trans. Commun.*, vol. COM-33, pp. 1094–1099, Sept. 1994.

[5] R. Beltran, F. H. Raab, and A. Velazquez, "HF outphasing transmitter using class-E power amplifiers," in *IEEE Int'l Microwave Symp.*, 2009, pp. 757–760.

[6] S. Moloudi, K. Takinami, M. Youssef, M. Mikhemar, and A. Abidi, "An outphasing power amplifier for a software-defined radio transmitter," *Proc. Int. Solid-State Circuits Conf. Tech. Dig.*, pp. 568–636, Feb. 2008.

[7] J. Yao and S. I. Long, "Power amplifier selection for LINC applications," *IEEE Trans. Circuits Syst. II*, vol. 53, no. 8, pp. 763–767, Aug. 2006.

[8] H. Xu, Y. Palaskas, A. Ravi, M. Sajadieh, M. El-Tanani, and K. Soumyanath, "A flip-chip-packaged 25.3 dBm class-D outphasing power amplifier in 32 nm CMOS for WLAN application," *IEEE J. Solid-State Circuits*, vol. 46, no. 7, pp. 1596–1605, 2011.

[9] S. Kee, I. Aoki, A. Hajimiri, and D. Rutledge, "The class E/F family of ZVS switching amplifiers," *IEEE Trans. Microwave Theory and Tech.*, vol. 51, no. 6, pp. 1677–1690, June 2003.

[10] F. H. Raab, P. Asbeck, S. Cripps, P. Kenington, Z. Popovich, N. Pothecary, J. Sevic, and N. Sokal, "RF and microwave power amplifier and transmitter technologies – part 2," *High Frequency Electronics*, pp. 22–36, May 2003.

[11] L. R. Kahn, "Single-sideband transmission by envelope elimination and restoration," *Proc. of the IRE*, vol. 40, no. 7, pp. 803–806, July 1952.

[12] V. Petrovic and W. Gosling, "Polar-loop transmitter," *Proc. of the IRE*, vol. 15, no. 10, pp. 286–288, May 1979.

[13] P. Reynaert and M. S. J. Steyaert, "A 1.75-GHz polar modulated CMOS RF power amplifier for GSM-EDGE," *IEEE J. Solid-State Circuits*, vol. 40, no. 12, pp. 2598–2608, Dec. 2005.

[14] F. Wang, , D. Kimball, J. Popp, A. Yang, D. Lie, P. Asbeck, and L. Larson, "Wideband envelope elimination and restoration power amplifier with high efficiency wideband envelope amplifier for WLAN 802.11g applications," in *Proc. IEEE Int'l Microwave Symp.*, 2005, pp. 645–648.

[15] J. S. Walling, S. S. Taylor, and D. J. Allstot, "A class-G supply-modulator and class-E PA in 130 nm CMOS," *IEEE J. Solid-State Circuits*, vol. 44, no. 9, pp. 2339–2347, Sept. 2009.

[16] A. Shameli, A. Safarian, A. Rofougaran, M. Rofougaran, and F. D. Flaviis, "A two-point modulation technique for CMOS power amplifier," *IEEE Trans. Microwave Theory Tech.*, vol. 55, no. 1, pp. 31–38, Jan. 2008.

[17] J. Choi, D. Kim, D. Kang, M. Jun, B. Jin, J. Park, and B. Kim, "A 45/46/34% PAE linear polar transmitter for EDGE/WCDMA/Mobile-WiMAX," in *Proc. IEEE RFIC Symp.*, 2009.

[18] J. Choi, J. Yim, J. Yang, J. Kim, J. Cha, and B. Kim, "Delta-Sigma digitized RF transmitter," in *Proc. IEEE Int'l Microwave Symp.*, 2007, pp. 81–84.

[19] S. Chung, P. A. Godoy, T. W. Barton, E. W. Huang, D. J. Perreault, and J. L. Dawson, "Asymmetric multilevel outphasing architecture for multistandard transmitters," in *Proc. IEEE RFIC Symp.*, 2009, pp. 237–240.

[20] J. Hur, O. Lee, K. Kim, K. Lim, and J. Laskar, "Highly efficient uneven multi-level LINC transmitter," *Electronic Letters*, pp. 837–838, July 2009.

[21] S. Chung, P. A. Godoy, T. W. Barton, E. W. Huang, D. J. Perreault, and J. L. Dawson, "Asymmetric multilevel outphasing transmitter using class-E PAs with discrete pulse width modulation," in *IEEE Int'l Microwave Symp.*, 2010, pp. 264–267.

[22] P. A. Godoy, S. Chung, T. W. Barton, D. J. Perreault, and J. L. Dawson, "A 2.5-GHz asymmetric multilevel outphasing power amplifier in 65-nm CMOS," in *IEEE Power Amplifiers for Wireless and Radio Applications (PAWR)*, Jan. 2011, pp. 57–60.

[23] ——, "A highly efficient 1.95-GHz, 18-W asymmetric multilevel outphasing transmitter for wideband applications," in *IEEE Int'l Microwave Symp.*, 2011, pp. 1–4.

[24] M.-H. Huang and K.-H. Chen, "Single-inductor multi-output (SIMO) DC-DC converters with high light-load efficiency and minimized cross-regulation for portable devices," *IEEE J. Solid-State Circuits*, vol. 44, no. 4, pp. 1099–1111, Apr. 2009.

[25] D. Y. C. Lie, J. D. Popp, F. Wang, D. Kimball, and L. E. Larson, "Linearization of highly-efficieny monolithic class E SiGe power amplifiers with envelope-tracking (ET) and envelope-elimination-and-restoration (EER) at 900MHz," in *Proc. IEEE Dallas Circuits and Systems Workshop on System-on-Chip*, Nov. 2007.

[26] S. Chung, J. W. Holloway, and J. L. Dawson, "Energy-efficiency digital predistortion with lookup table training using analog Cartesian feedback," *IEEE Trans. Microwave Theory Tech.*, pp. 2248–2258, Oct. 2009.

[27] J. Mehta *et al.*, "An efficient linearization scheme for a digital polar EDGE transmitter," *IEEE Trans. Circuits Syst. II*, vol. 57, no. 3, pp. 193–197, Mar. 2010.

[28] A. Phan, G. W. Wornell, and C. G. Sodini, "A digital amplitude-to-phase conversion for high efficiency linear outphase

power amplifiers," in *Proc. IEEE Int'l Conf. on Acoustics, Speech, and Signal Processing*, vol. 4, Toulouse, France, May 2006, pp. 97–100.

[29] A. Pham, "Outphase power amplifiers in OFDM systems," PhD Dissertation, Massachusetts Institute of Technology, Sept. 2005.

[30] M. Acar, M. P. van der Heijden, I. Volokhine, M. Apostolidou, J. Sonsky, and J. S. Vromans, "Scalable CMOS power devices with 70% PAE and 1, 2 and 3.4 watt output power at 2GHz," in *Proc. IEEE RFIC Symp.*, June 2009, pp. 233–236.

[31] M. Acar, A. Annema, and B. Nauta, "Variable-voltage class-E power amplifiers," in *Proc. IEEE Int'l Microwave Symp.*, June 2007, pp. 1095–1098.

[32] M. Apostolidou, M. P. van der Heijden, D. M. W. Leenaerts, J. Sonsky, A. Heringa, and I. Volokhine, "A 65nm CMOS 30dBm class-E power amplifier with 60% power added efficiency," in *Proc. IEEE RFIC Symp.*, 2008, pp. 141–144.

[33] ——, "A 65 nm CMOS 30 dBm class-E RF power amplifier with 60% PAE and 40% PAE at 16 dB back-off," *IEEE J. Solid-State Circuits*, vol. 44, no. 5, pp. 1372–1379, May 2009.

[34] D. Chowdhury, C. Hull, O. Degani, P. Goyal, Y. Wang, and A. Niknejad, "A single-chip highly linear 2.4GHz 30dBm power amplifier in 90nm CMOS," *Proc. Int. Solid-State Circuits Conf. Tech. Dig.*, pp. 378–379, Feb. 2009.

[35] J. Kang, A. Hajimiri, and B. Kim, "A single-chip linear CMOS power amplifier for 2.4GHz WLAN," *Proc. Int. Solid-State Circuits Conf. Tech. Dig.*, pp. 208–209, Feb. 2006.

[36] T. W. Barton, S. Chung, P. A. Godoy, D. J. Perreault, and J. L. Dawson, "A 12-bit resolution, 200-MSample/second phase modulator for a 2.5ghz carrier with discrete carrier pre-rotation in 65nm cmos," in *Proc. IEEE RFIC Symp.*, June 2011.

[37] S. Yoo, J. Walling, E. Woo, B. Jann, and D. Allstot, "A switched-capacitor RF power amplifier," *IEEE J. Solid-State Circuits*, vol. xx, no. yy, pp. 1–11, 2011.

[38] O. Degani, F. Cossoy, S. Shahaf, D. Chowdhury, C. Hull, C. Emanuel, and R. Shmuel, "A 90nm CMOS power amplifier for 802.16e (WiMAX) applications," in *Proc. IEEE RFIC Symp.*, June 2009.

[39] A. Afsahi, A. Behzad, V. Magoon, and L. Larson, "Fully integrated dual-band power amplifiers with on-chip baluns in 65nm CMOS for an 802.11n MIMO WLAN SoC," in *Proc. IEEE RFIC Symp.*, June 2009.

[40] D. Chowdhury, S. Thyagarajan, L. Ye, E. Alon, and A. Niknejad, "A fully-integrated efficient CMOS inverse class-D power amplifier for digital polar transmitters," in *Proc. IEEE RFIC Symp.*, June 2011.

[41] W. Tai, H. Xu, A. Ravi, H. Lakdawala, O. Degani, L. Carley, and Y. Palaskas, "A 31.5dBm outphasing class-D power amplifier in 45nm CMOS with back-off efficiency enhancement by dynamic power control," in *Proc. IEEE ESSCIRC*, Sept. 2011, pp. 131–134.

IEEE Journal of Solid-State Circuits, Vol. 47, No. 10, pp. 2372-2384, Oct. 2012.

Philip Godoy (S'05–M'12) received the B.S. degree in electrical engineering and computer science from the University of California, Berkeley, in 2006 and the S.M. and Ph.D. degrees in electrical engineering from the Massachusetts Institute of Technology (MIT), Cambridge, in 2008 and 2011, respectively.

He did a summer internship on data converters with Broadcom Corporation in San Jose, CA in 2006. He has been with Marvell Semiconductor, Santa Clara, CA, since August 2011. His main research interests include RF, analog, and digital circuits, particularly digitally-assisted RF systems.

SungWon Chung (S'99) received the B.S. degree from Pusan National University in 2002 and the M.S. degree from KAIST in 2005. He is currently working towards the Ph.D. degree at MIT. During the summer of 2008, he worked as a design engineering intern at Intersil in Milpitas, CA, involved in high-speed communication transceiver chipset design.

Taylor Barton received the S.B., M.Eng., and Electrical Engineer degrees in 2006, 2008, and 2010 respectively from the Massachusetts Institute of Technology, Cambridge, where she is currently pursuing the Ph.D. degree in electrical engineering.

Her research interests are in RF and analog circuit design and classical control theory.

IEEE Journal of Solid-State Circuits, Vol. 47, No. 10, pp. 2372-2384, Oct. 2012.

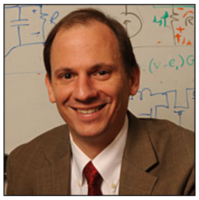

David J. Perreault (S'91, M'97, SM '06) received the B.S. degree from Boston University, Boston, MA, and the S.M. and Ph.D. degrees from the Massachusetts Institute of Technology, Cambridge, MA. In 1997 he joined the MIT Laboratory for Electromagnetic and Electronic Systems as a Postdoctoral Associate, and became a Research Scientist in the laboratory in 1999. In 2001, he joined the MIT Department of Electrical Engineering and Computer Science, where he is presently Professor of Electrical Engineering. His research interests include design, manufacturing, and control techniques for power electronic systems and components, and in their use in a wide range of applications. Dr. Perreault received the Richard M. Bass Outstanding Young Power Electronics Engineer Award from the IEEE Power Electronics Society, an ONR Young Investigator Award, and the SAE Ralph R. Teetor Educational Award, and is co-author of four IEEE prize papers.

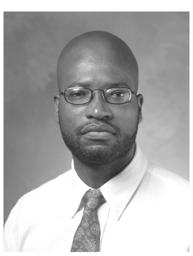

Joel L. Dawson (S'96–M'04) is an associate professor in the Department of Electrical Engineering and Computer Science at MIT. He received the S.B. in EE from MIT in 1996, and the MEng. degree from MIT in EECS in 1997. He went on to pursue further graduate studies at Stanford University, where he received his Ph.D. in Electrical Engineering for his work on power amplifier linearization techniques. Before joining the faculty at MIT, Dr. Dawson spent one year at Aspendos Communications, a startup company that he co-founded. He received the NSF CAREER award in 2008, and was selected for the Presidential Early Career Award for Scientists and Engineers (PECASE) in 2009. Prof. Dawson is the CTO and founder of Eta Devices, Inc., a startup company based in Cambridge, MA.

IEEE Journal of Solid-State Circuits, Vol. 47, No. 10, pp. 2372-2384, Oct. 2012.

LIST OF FIGURES

IEEE Journal of Solid-State Circuits, Vol. 47, No. 10, pp. 2372-2384, Oct. 2012.

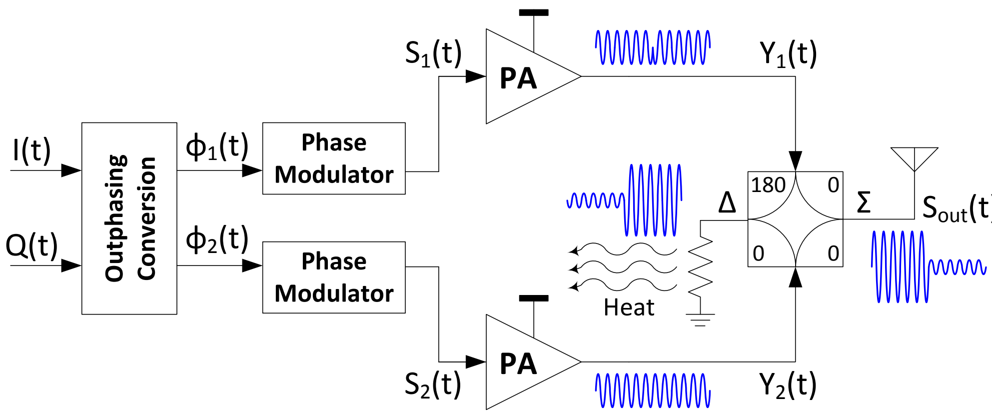

(a)

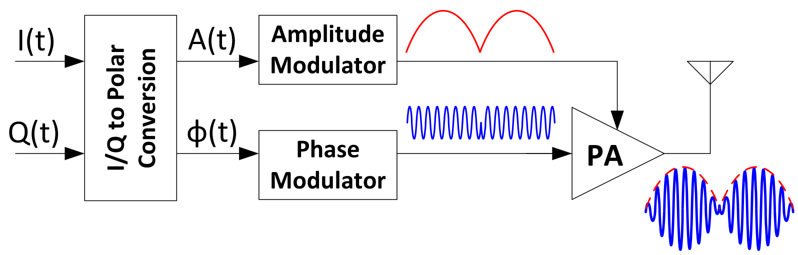

(b)

Fig. 1. (a) Conventional outphasing, or LINC, architecture. (b) Conventional polar architecture.

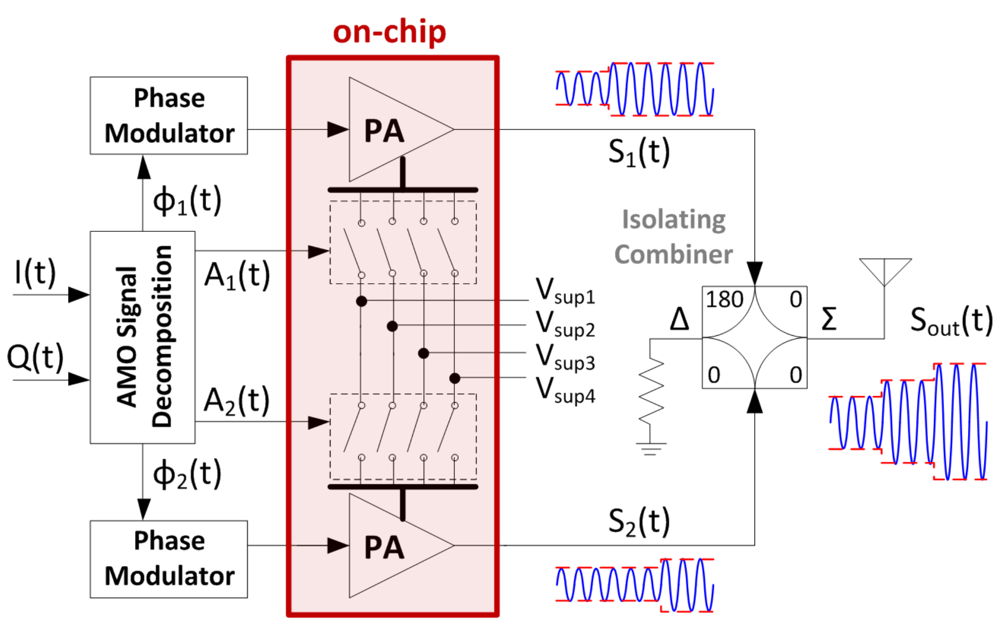

Fig. 2. Asymmetric multilevel outphasing (AMO) transmitter with 4-level discrete supply-voltage modulation.

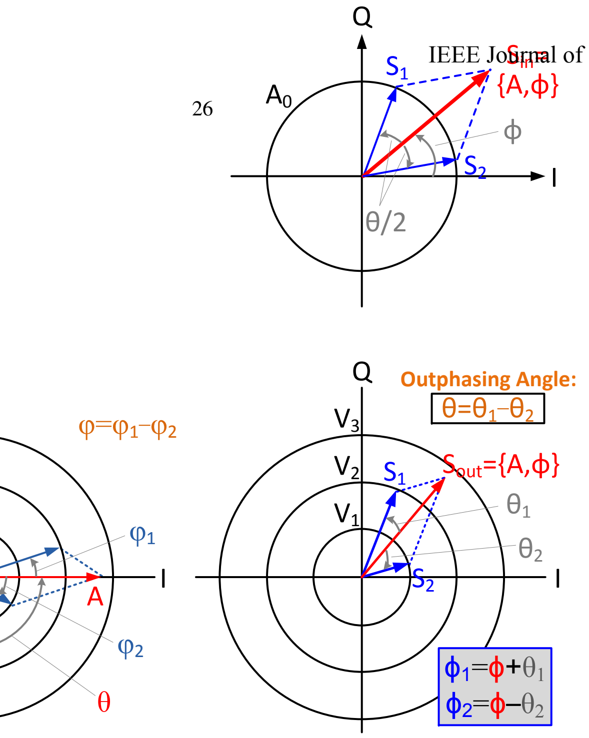

Fig. 3. Vector diagram for AMO modulation, including notational convention.

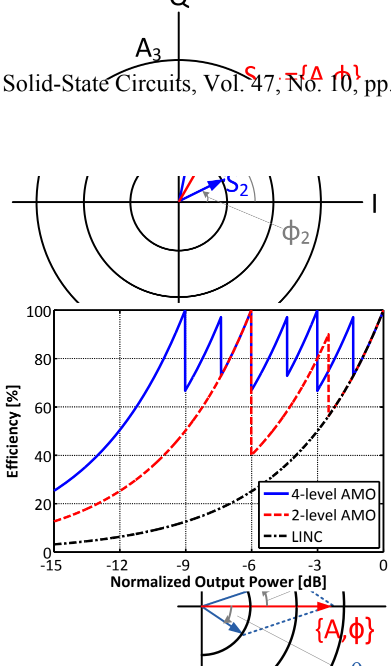

Fig. 4. Efficiency vs. output power of AMO modulation when there are 4 amplitude levels available vs. when there are 2 amplitude levels available, assuming 100% efficiency in the PAs. The efficiency of LINC is also shown for comparison.

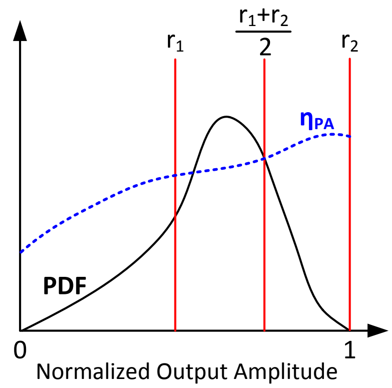

Fig. 5. Example amplitude PDF for a signal, along with an example PA efficiency curve η_{PA} vs. output amplitude. The r_k are the maximum output amplitudes for each of the different supply voltage levels $V_{sup,k}$ when both PAs are driven by the same supply. There are 2 amplitude levels available in the example above.

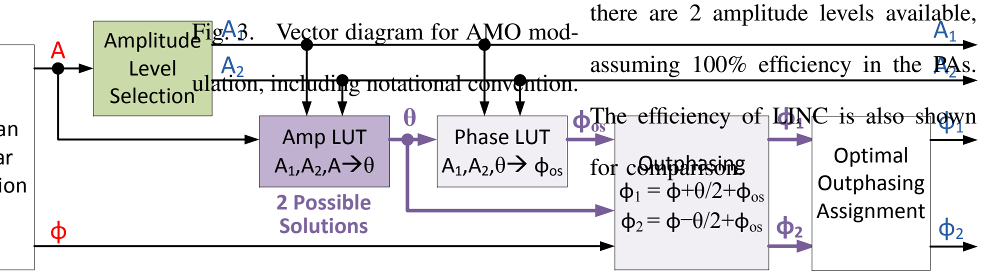

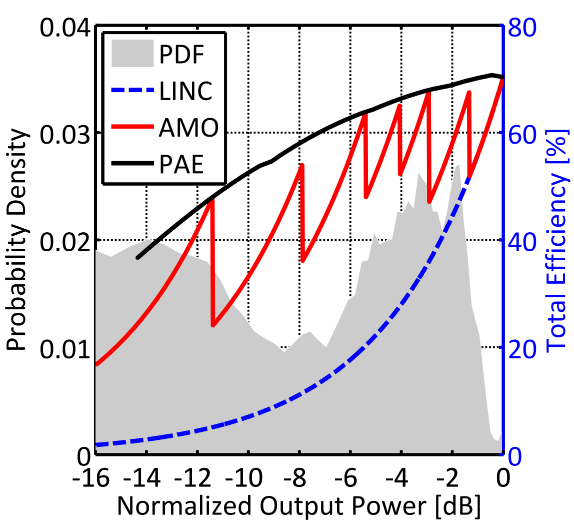

(a) HSUPA

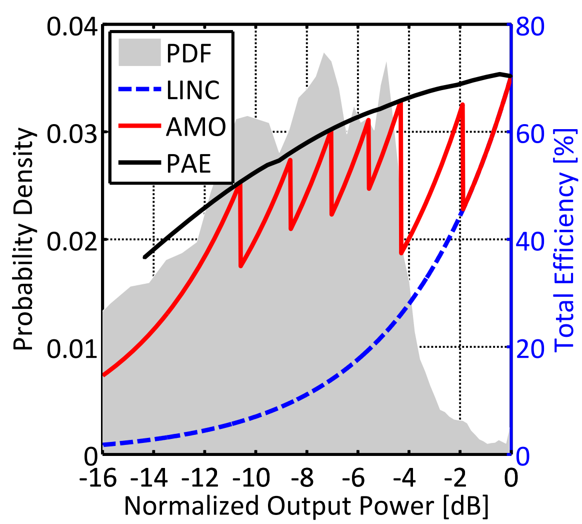

(b) WLAN

Fig. 6. Amplitude PDF of a modulated signal and corresponding optimum efficiency curves for LINC and AMO with 4 available supply voltages. (a) HSUPA signal. (b) WLAN signal.

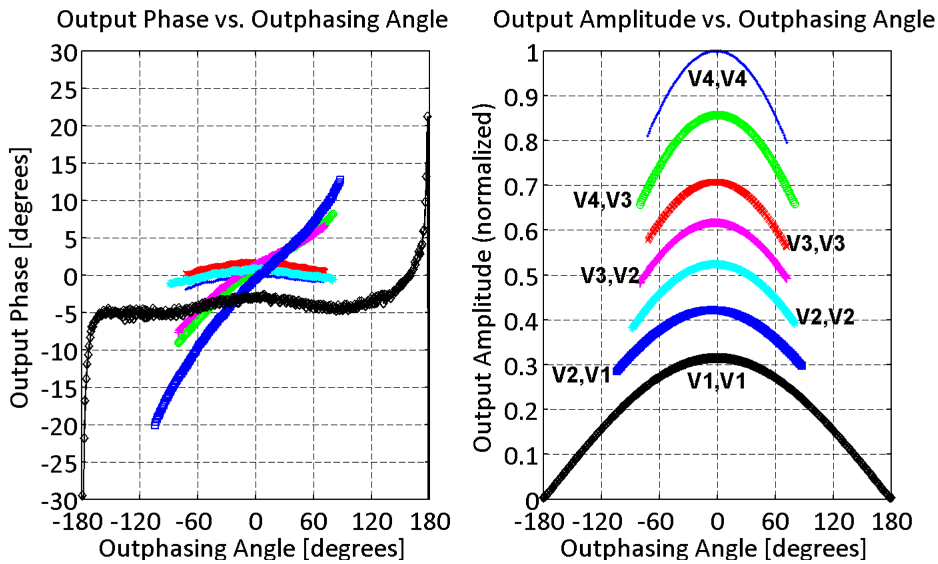

Fig. 7. Measured static output amplitude and phase vs. outphasing angle for the 2.4-GHz AMO PA, which capture the static nonlinearities of the AMO system. Each curve corresponds to a different combination of supply voltages for the two outphased PAs.

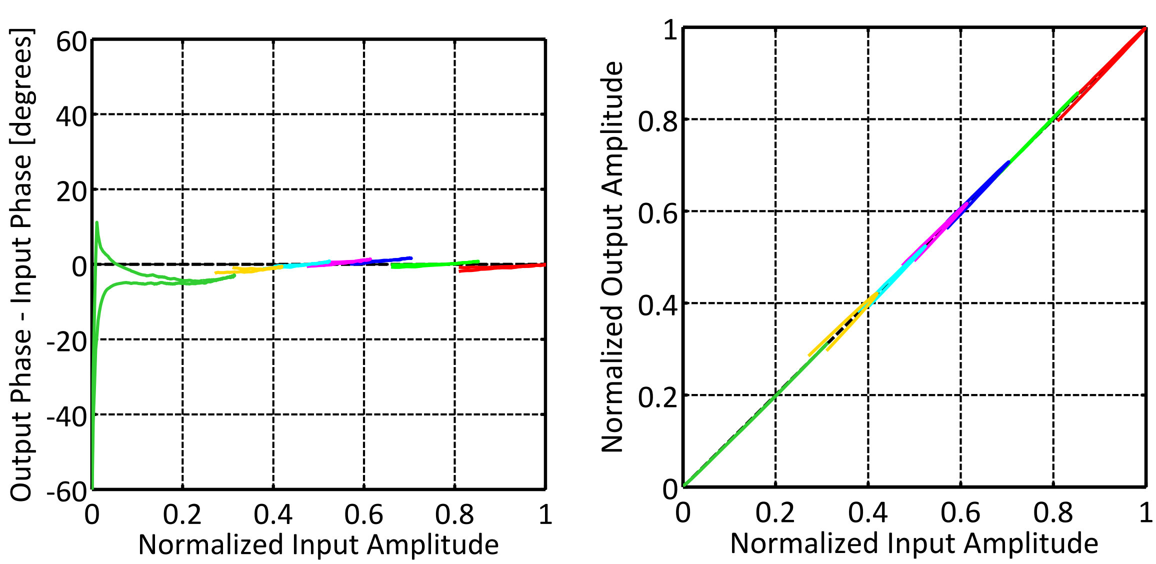

(a) AM-PM

(b) AM-AM

Fig. 8. Amplitude and phase linearity plots for the measurement data given in Fig. 7. (a) Difference between the measured output phase and the ideal input phase, plotted vs. the ideal input amplitude. (b) Measured output amplitude vs. the ideal input amplitude. The ideal input amplitudes and phases are the result from the ideal AMO signal decomposition given in Section II-A.

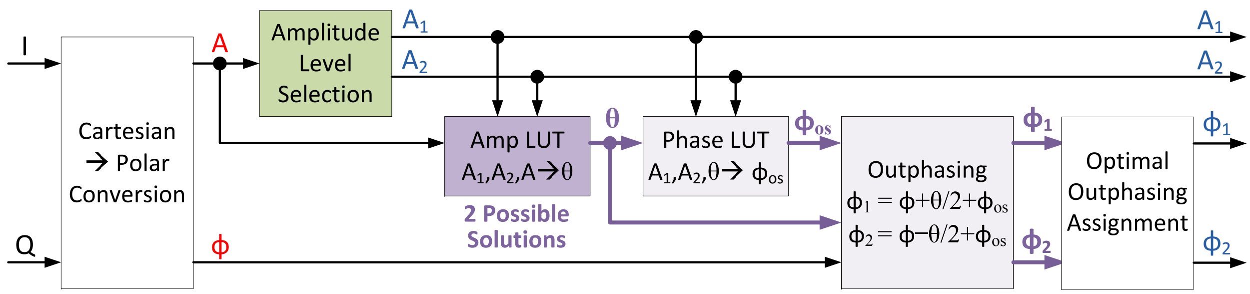

Fig. 9. Block diagram for the AMO signal decomposition with DPD based on lookup tables.

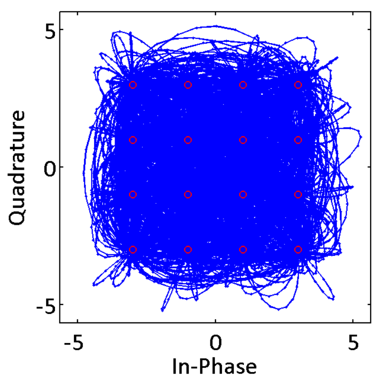

(a) 16-QAM input data

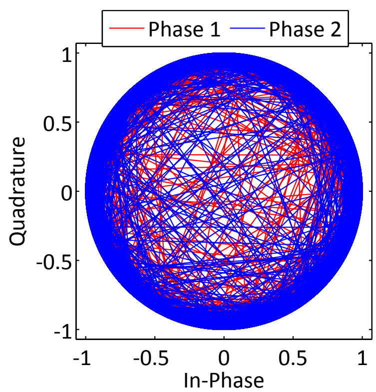

(b) PA phases w/o optimal assignment

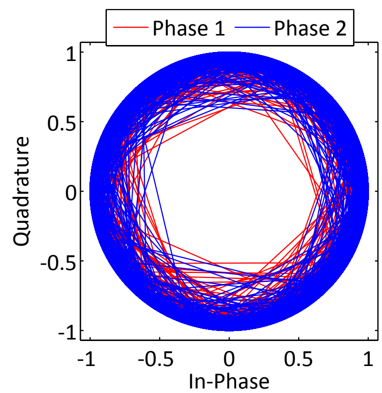

(c) PA phases with optimal assignment

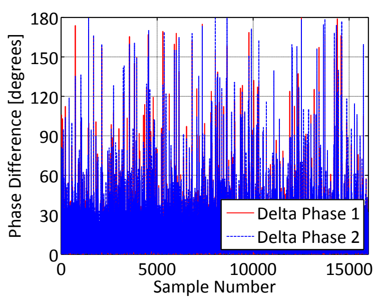

(d) Non-optimal phase differences

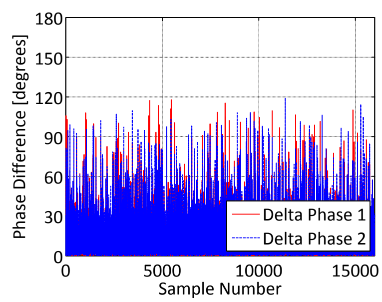

(e) Optimal phase differences

Fig. 10. The PA phases and phase differences after the AMO signal decomposition with and without the optimal outphasing assignment.

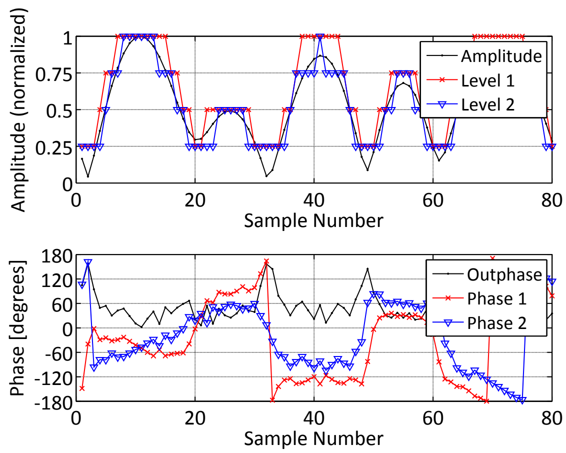

Fig. 11. Time-domain waveforms of the PA amplitudes and phases resulting from the AMO signal decomposition with DPD, A_1, A_2, ϕ_1, ϕ_1, for a segment of the 16-QAM signal shown in Fig. 10(a), using the measured data shown in Fig. 7. The amplitude of the input signal and the outphasing angle between the two PAs is also shown.

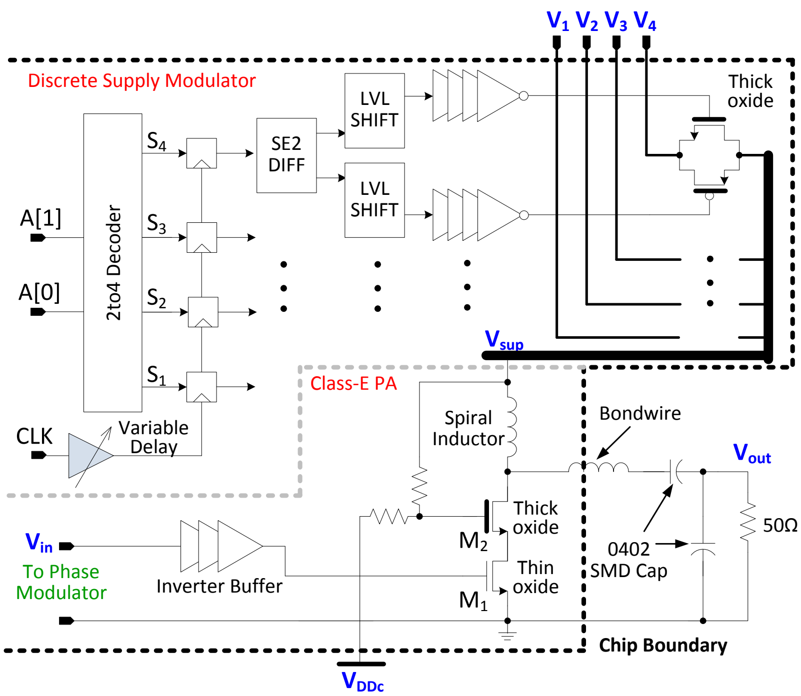

Fig. 12. Circuit schematic of the 4-level discrete supply modulator and class-E PA used in the AMO system. The single-ended version of the PA is shown for simplicity, but the PA is differential on chip.

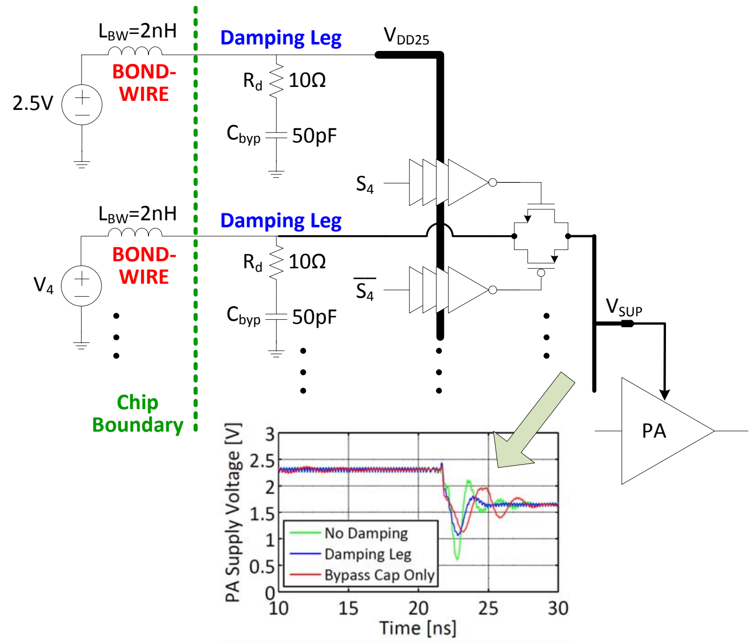

Fig. 13. Discrete supply modulator with damping legs to reduce the transient ringing on the on-chip supply voltage nodes. The simulated transient waveforms of the power supply ringing with and without the damping leg are also shown.

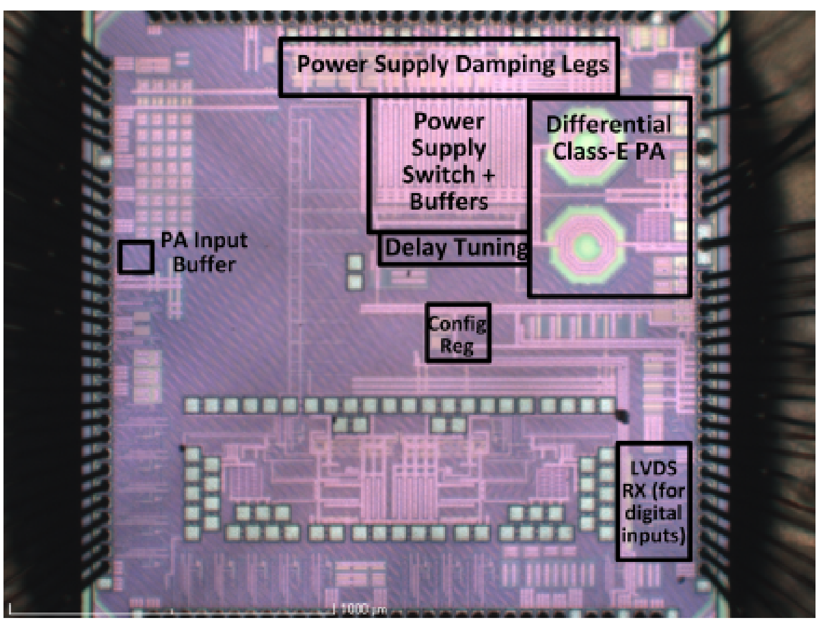

Fig. 14. Die photo of the PA and discrete supply modulator used in the 2.4-GHz AMO PA. The total chip area is 2x2 mm^2, but the active area of the chip used for the class-E PA, discrete supply-voltage modulator, buffers, and digital logic is about 1×1 mm^2.

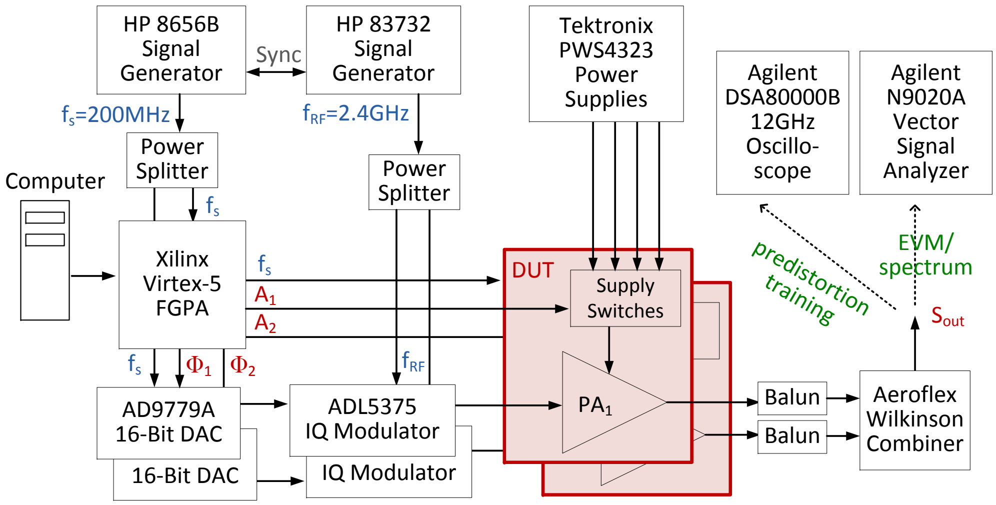

Fig. 15. Testbench for the 2.4-GHz AMO PA, composed of two CMOS class-E PAs and two discrete supply modulators.

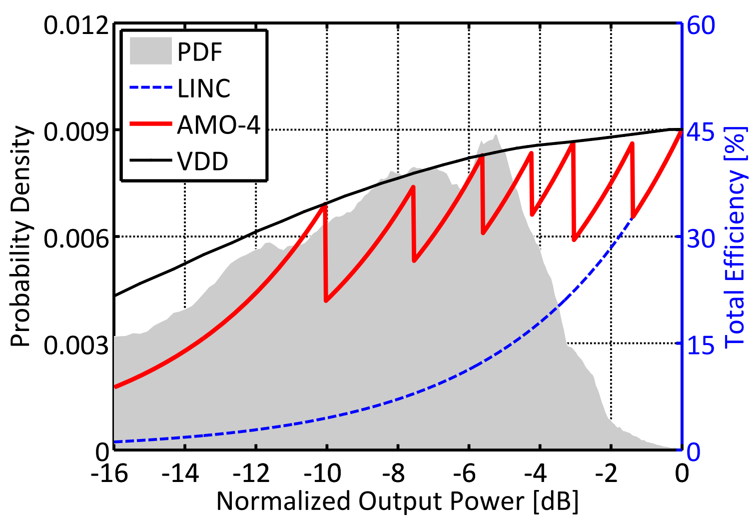

Fig. 16. Measured efficiency vs. output power for the 2.4-GHz AMO PA, along with the optimized amplitude levels for a 64-QAM signal with 7.0-dB PAPR. The PDF of the 64-QAM signal is also shown.

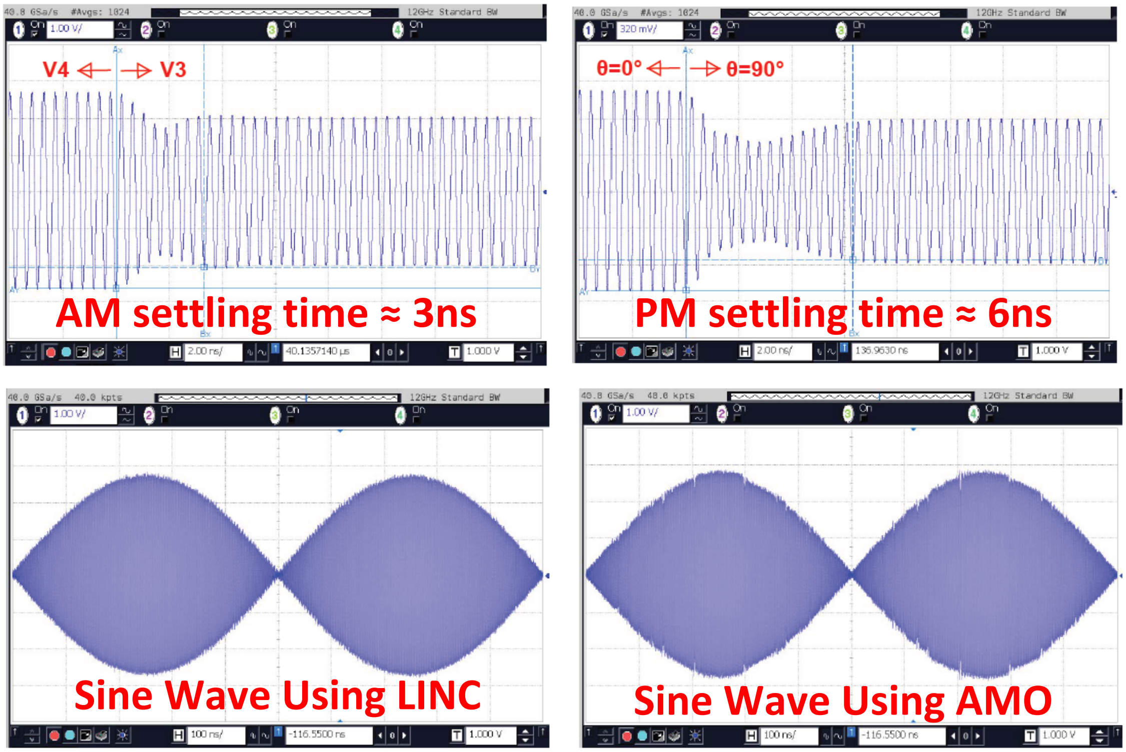

Fig. 17. Measured AM and PM step responses of the AMO PA output, and measured output waveforms for a 1-MHz baseband sine wave transmission.

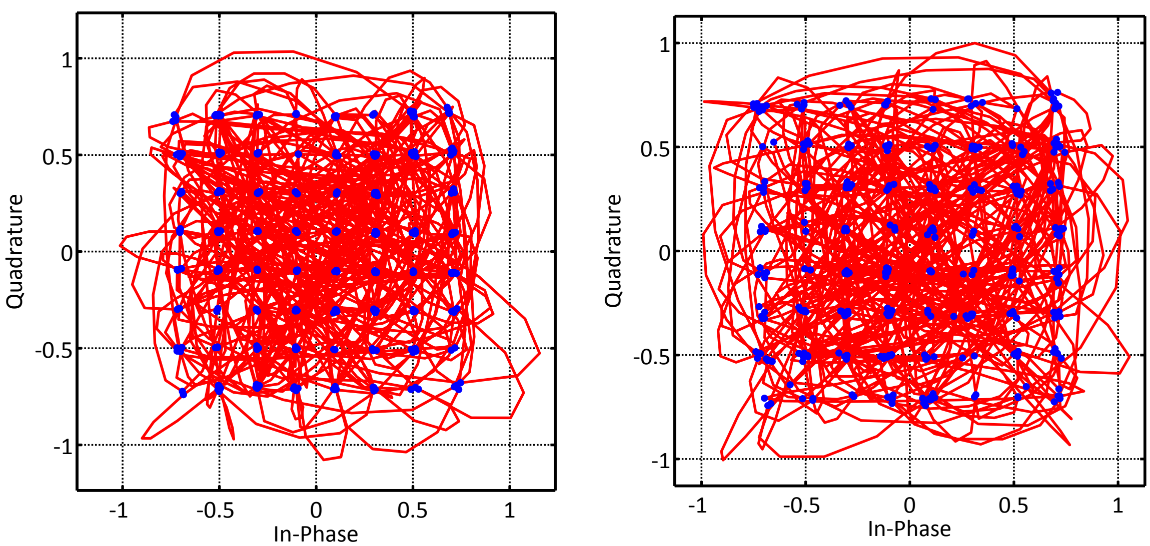

(a) 10-MHz 64-QAM, EVM=1.2%

(b) 40-MHz 64-QAM, EVM=2.5%

Fig. 18. Constellation diagram of a 64-QAM signal transmitted by the AMO system at various symbol rates for the 2.4-GHz AMO PA. (a) 10 MHz. (b) 40 MHz.

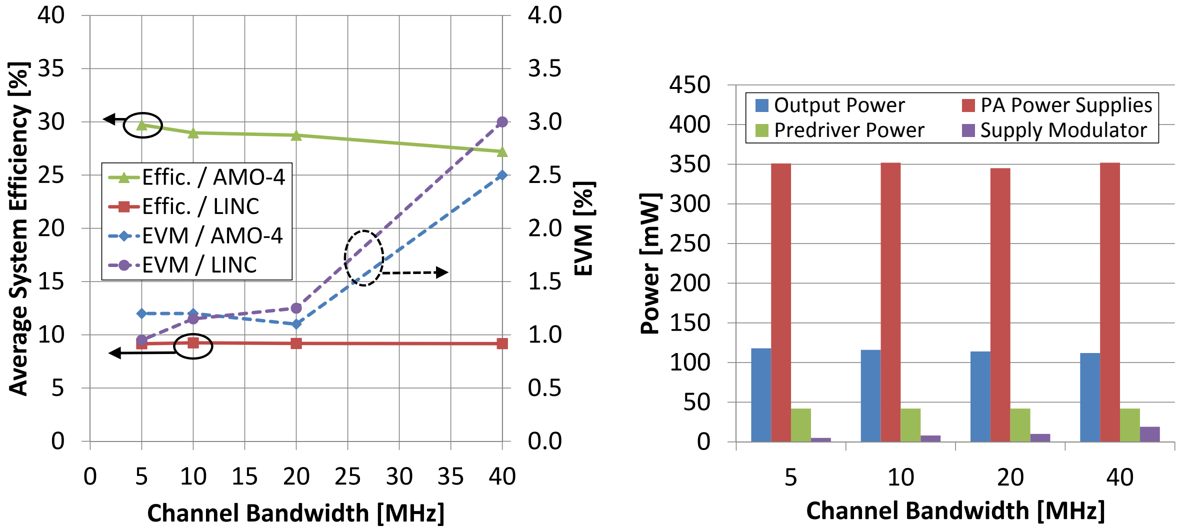

(a) Efficiency, EVM

(b) Power Breakdown

Fig. 19. Average system efficiency, EVM (a) and power breakdown (b) of the 2.4-GHz AMO PA for the transmission of a 7.0-dB PAPR 64-QAM signal at various channel bandwidths.

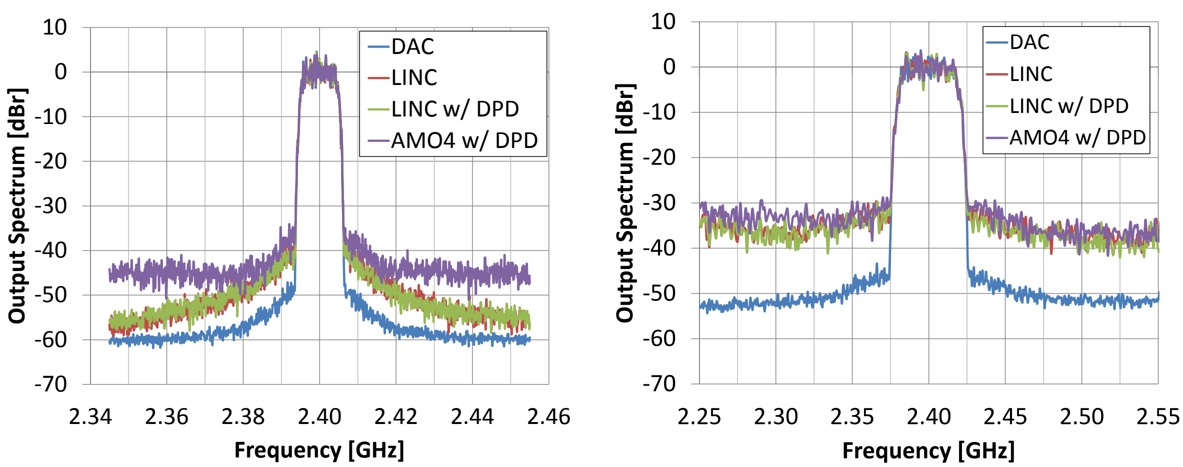

(a) 10 MHz

(b) 40 MHz

Fig. 20. Transmit spectrum of a 64-QAM signal transmission at 10-MHz (a) and 40-MHz (b) symbol rates.

IEEE Journal of Solid-State Circuits, Vol. 47, No. 10, pp. 2372-2384, Oct. 2012.

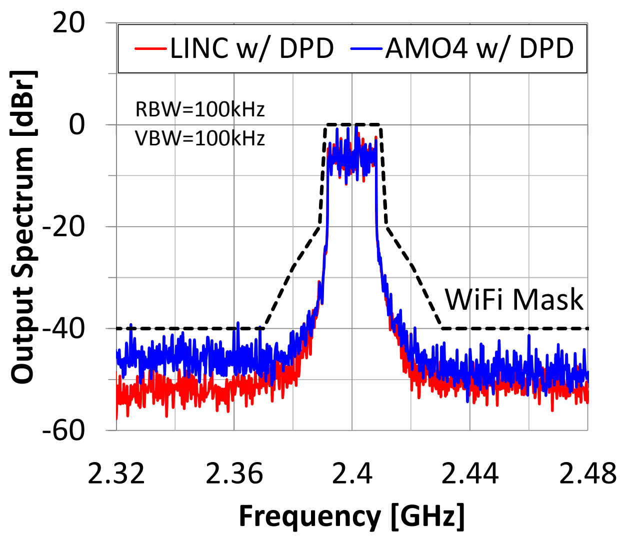

(a) Output Spectrum

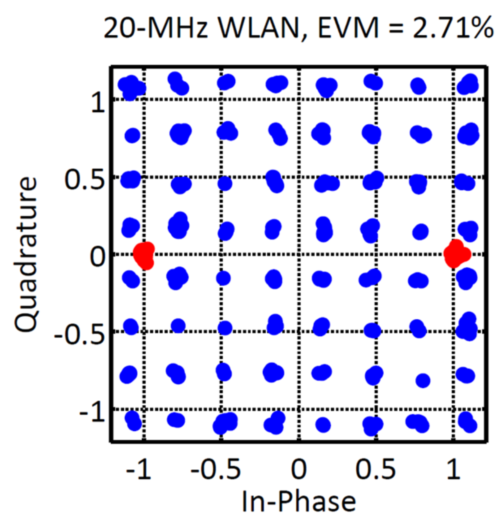

(b) Constellation

Fig. 21. Transmit spectrum (a) and constellation diagram (b) for a 20-MHz 64-QAM OFDM signal.

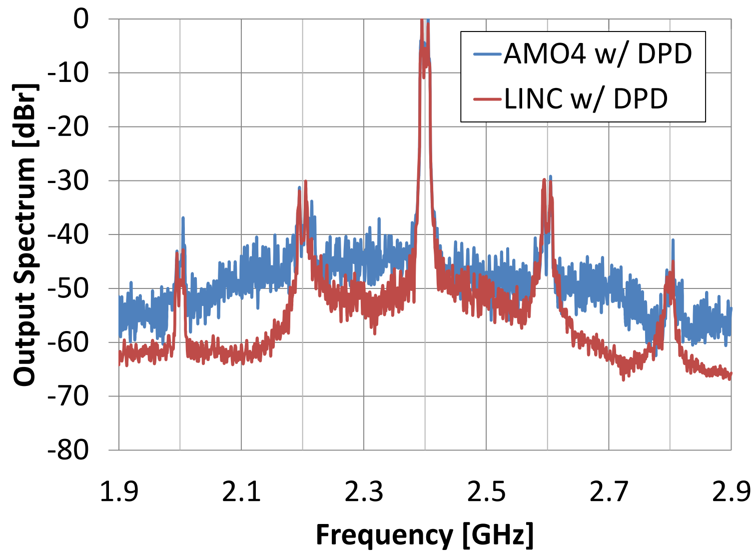

Fig. 22. Wideband output spectrum for the 20-MHz 64-QAM OFDM signal transmission shown in Fig. 21.

IEEE Journal of Solid-State Circuits, Vol. 47, No. 10, pp. 2372-2384, Oct. 2012.

LIST OF TABLES

TABLE I

PERFORMANCE COMPARISON OF THIS WORK WITH STATE-OF-THE-ART

System Architecture	Tech.	Carrier Freq	Bandwidth	Modulation	PAPR	Peak P_{out}	Avg P_{out}	Peak PAE	Avg PAE
AMO [This Work]	65 nm	2.4 GHz	20 MHz	OFDM	7.5 dB	27.7 dBm	20.2 dBm	45.1%	27.6%
Switched-cap PA [37]	90 nm	2.25 GHz	20 MHz	OFDM	7.5 dB	25.2 dBm	17.7 dBm	45.0%	27.0%
Class-AB [38]	90 nm	2.5 GHz	10 MHz	WiMAX	7.0 dB	32.0 dBm	25.0 dBm	48.0%	25.0%
Class-AB [39]	65 nm	2.442 GHz	20 MHz	OFDM	5.9 dB	28.3 dBm	22.4 dBm	35.3%†	23.2%†
Class-G Polar [15]	130 nm	2.0 GHz	20 MHz	OFDM	9.7 dB	29.3 dBm	19.6 dBm	69.0%	22.6%
Outphasing [8]	32 nm	2.4 GHz	20 MHz	OFDM	5.8 dB	25.3 dBm	19.6 dBm	35.0%	21.8%
Inverse Class-D [40]	65 nm	2.25 GHz	20 MHz	OFDM	7.8 dB	21.8 dBm	14.0 dBm	44.2%†	18.0%†
Outphasing [41]	45 nm	2.4 GHz	20 MHz	OFDM	6.7 dB	31.5 dBm	24.8 dBm	27.0%	16.0%

†Drain Efficiency, not PAE